



## BIOMIMETICS

# An ultrawide field-of-view pinhole compound eye using hemispherical nanowire array for robot vision

Yu Zhou<sup>1,2†</sup>, Zhibo Sun<sup>1,2†</sup>, Yucheng Ding<sup>1,2†</sup>, Zhengnan Yuan<sup>1,2</sup>, Xiao Qiu<sup>1,2</sup>, Yang Bryan Cao<sup>1,2</sup>, Zhu'an Wan<sup>1</sup>, Zhenghao Long<sup>1,2</sup>, Swapnadeep Poddar<sup>1</sup>, Shivam Kumar<sup>1,2</sup>, Wenhao Ye<sup>1</sup>, Chak Lam Jonathan Chan<sup>1</sup>, Daquan Zhang<sup>1,2</sup>, Beita Ren<sup>1,2</sup>, Qianpeng Zhang<sup>1,2</sup>, Hoi-Sing Kwok<sup>1,2</sup>, Mitch Guijun Li<sup>1,2,3</sup>, Zhiyong Fan<sup>1,2,4,5\*</sup>

Copyright © 2024 the Authors, some rights reserved; exclusive licensee American Association for the Advancement of Science. No claim to original U.S. Government Works

Garnering inspiration from biological compound eyes, artificial vision systems boasting a vivid range of diverse visual functional traits have come to the fore recently. However, most of these artificial systems rely on transformable electronics, which suffer from the complexity and constrained geometry of global deformation, as well as potential mismatches between optical and detector units. Here, we present a unique pinhole compound eye that combines a three-dimensionally printed honeycomb optical structure with a hemispherical, all-solid-state, high-density perovskite nanowire photodetector array. The lens-free pinhole structure can be designed and fabricated with an arbitrary layout to match the underlying image sensor. Optical simulations and imaging results matched well with each other and substantiated the key characteristics and capabilities of our system, which include an ultrawide field of view, accurate target positioning, and motion tracking function. We further demonstrate the potential of our unique compound eye for advanced robotic vision by successfully completing a moving target tracking mission.

## INTRODUCTION

Evolution has created diverse natural biological vision systems (1). Specifically, natural compound eyes with extraordinary visual capabilities (table S1), such as wide field of view (FoV) and rapid motion tracking (2, 3), offer tremendous attraction for practical applications, particularly for robotic systems. Inspired by this, numerous artificial compound eyes have been extensively explored, most of which are fabricated by transferring a microlens array onto curved substrates and subsequently integrating them with commercial planar image sensors (4–6). In these cases, the imaging ability of compound eyes is severely limited by the tricky transfer process, which makes it difficult to control uniformity and inevitably leads to mismatches between three-dimensional (3D) optical structures and underlying planar commercial imagers. To ameliorate the issue, two promising strategies based on advanced micro-nano fabrication and soft electronics have been explored. One approach involved precisely shaping optical structures with a microlens array on curved surfaces through photopolymerization (7, 8), laser writing (9, 10), laser-assisted etching (11, 12), microfluid-assisted molding (13, 14), or 3D printing (15, 16). These optical structures were further assembled on planar imagers with the aid of complex waveguide units and costly lens systems. In the other approach, deformable electronics enabled the entire compound system to be transformed into curvy shapes via elastomeric transfer (17–20), origami (21), or kirigami (22, 23). The

deformation process partially addressed the mismatch problem but still faced challenges related to deformation stability, limited pixel numbers, and large unused space between imaging pixels for stress release. For example, direct deformation into hemispherical configuration generates substantial residual stress, which poses a risk of mechanical instability for a working compound eye. Hindered by the abovementioned bottlenecks, there are very few reports on the functional demonstration of compact compound eye systems integrated into autonomous platforms such as robots or drones (24, 25).

In this study, we demonstrate a lens-free artificial compound eye vision system (Movie 1) composed of a 3D-printed pinhole array optical component and an inherently convex hemispherical image sensor containing a high-density perovskite nanowire array (PNA). The pinhole array was meticulously designed and shaped in honeycombed anatomy, forming conformal contact with the underlying hemispherical imaging subsystem. The imager with PNA was further compositionally engineered to cover the visible and near-infrared spectral range with satisfactory performance. With the integrated pinhole compound eye (PHCE) system, we acquired ultrawide-angle panoramic images with an FoV of 140°. Furthermore, we implemented an advanced binocular PHCE system that features an expanded FoV of 220° and realizes stereopsis vision. With this system, we successfully achieved target positioning in 3D space. We demonstrated the functional integration of the PHCE system on a flying drone, enabling motion tracking of a quadruped on the ground. This unique air-ground collaborative robotic interaction showcases the potential of using our compound eye system for the development of multirobot collaboration and robot swarm technology in the future.

## RESULTS

### Design and fabrication of PHCE system

Figure 1A shows the schematic illustration of PHCE, including two primary components. In this device structure, the 3D-printed pinhole array serves as the lensless optical channels, aligning with the perovskite

<sup>1</sup>Department of Electronic & Computer Engineering, Hong Kong University of Science and Technology, Kowloon, Hong Kong SAR, China. <sup>2</sup>State Key Laboratory of Advanced Displays and Optoelectronics Technologies, Hong Kong University of Science and Technology, Kowloon, Hong Kong SAR, China. <sup>3</sup>Division of Integrative Systems and Design, Hong Kong University of Science and Technology, Kowloon, Hong Kong SAR, China. <sup>4</sup>Department of Chemical and Biological Engineering, Hong Kong University of Science and Technology, Kowloon, Hong Kong SAR, China. <sup>5</sup>Guangdong-Hong Kong-Macao Joint Laboratory for Intelligent Micro-Nano Optoelectronic Technology, Hong Kong University of Science and Technology, Hong Kong SAR, China.

\*Corresponding author. Email: eezfan@ust.hk

†These authors contributed equally to this work.

nanowire imager. As schematically displayed in Fig. 1B, perovskite nanowires grown inside hemispherical porous alumina membrane (PAM) serve as photoreceptors, and the residual lead (Pb) nanowires connected with metal wires function as visual signal transmission channels. Indium (In) was introduced to improve the contact between Pb and gallium (Ga). The typical perovskite nanowires inside PAM (pitch, ~500 nm; diameter, ~300 nm) can be observed in the scanning electron microscopy (SEM) image (Fig. 1C), indicating a uniform alignment with high density. The detailed fabrication process of the PHCE system is illustrated in figs. S1 and S2 and Supplementary Methods.

Inspired by the unique geometry of insects' compound eyes, such as the typical compound eye of a robber fly (Asilidae, Fig. 1D), we designed the honeycombed pinhole array and further fabricated the proof-of-concept PHCE with 121 ommatidia integrated on printed circuit boards (PCBs), as shown in Fig. 1E. In our case, the pinhole array optical structure is critical for the vision system. In particular, the diacritical acceptance angle ( $\Delta\phi$ , defined by the full width at half maximum of each pinhole's angular selective function), the inter-ommatidial angle ( $\Delta\Phi$ ), and limited pixel numbers synergistically dominate the image formation (26). The pinhole array layout (Fig. 1F and figs. S3 to S5) aims to eliminate the blind area between neighboring ommatidia while considering the overall geometry ( $\Delta\phi$  is slightly larger than  $\Delta\Phi$ ), as detailed in Supplementary Methods. Simulations on the intensity distributions of three adjacent pinholes with different length-diameter ratios ( $L/D$ ) and  $\Delta\Phi$  values (figs. S6 to S8) verify that the optimal parameters of pinhole array ( $L/D = 5$ ,  $\Delta\Phi = 10^\circ$ ) can eliminate the blind area between neighboring ommatidia and reduce the loss of light efficiency. Further optical simulations indicated that the total FoV of PHCE is  $\sim 143^\circ$  when  $\Delta\phi$  and  $\Delta\Phi$  are equal to  $11.3^\circ$  and  $10^\circ$ , respectively (Fig. 1G). We also measured the intensity distribution of a three-pinhole unit, as shown in Fig. 1H, which is in unity with the simulation result (fig. S6D). Furthermore, the light-absorbing resin was used for printing to thwart light scattering among adjacent pixels. Owing to the high printing freedom and simplified structure, the abovementioned parameters of pinhole array could be well designed and coordinated to meet the underlying imager's requirements (figs. S2E and S3D).

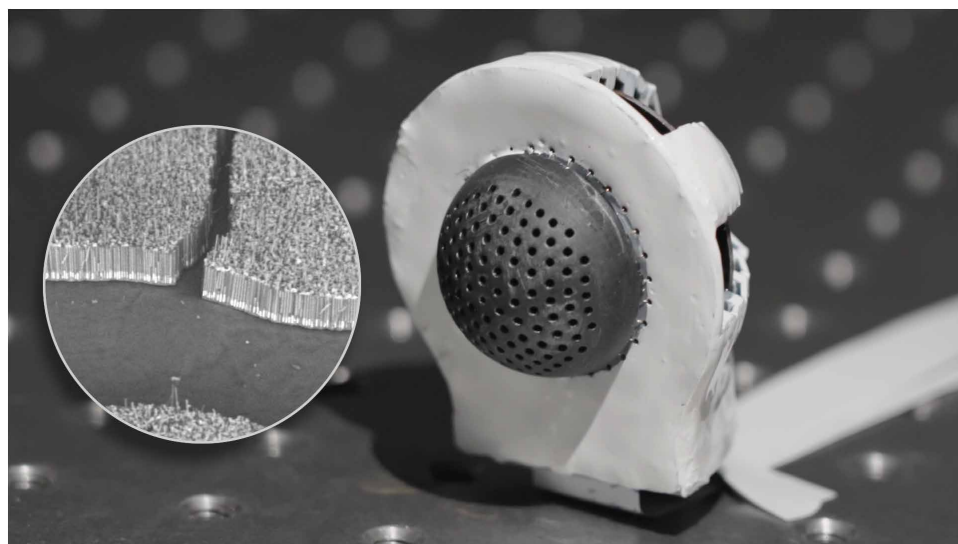
### Optoelectronic performance of PNA photodetector

The fabrication process of a typical PNA photodetector is schematically illustrated in fig. S1B. The vertical nanowire structure provides innate encapsulation for perovskite materials, elevating the operational performance. By regulating halide and metal elements in perovskite, the PNA photodetector can sense light from the visible to near-infrared regions, as evidenced by the variable peaks in the photoluminescence spectra (Fig. 2A). We further examined the x-ray diffraction (XRD) spectra of different perovskite nanowires inside PAM (Fig. 2B), in which diffraction peaks of well-crystalline perovskites shift with the substituted elements. In detail, the right shift of corresponding diffraction peaks results from the smaller halide atoms in the perovskite lattice. Elemental analysis displayed in fig. S9 further confirms the uniform growth of PNA in the PAM channels. We here chose methylammonium lead triiodide (MAPbI<sub>3</sub>) as photosensitive material for demonstration because it could encompass the entire visible wavelength range. In principle, other perovskite materials, such as all-inorganic counterparts, can also be used, as we reported previously (27–32). By tuning the PAM thickness and growth conditions, well-crystalline MAPbI<sub>3</sub> nanowires with a high filling ratio (>95%) inside PAM were obtained (fig. S10).

As depicted in Fig. 1B and Fig. 2C, we constructed a minimalistic photodetector with the configuration of In (1  $\mu\text{m}$ )/Pb (1  $\mu\text{m}$ )/MAPbI<sub>3</sub> (4  $\mu\text{m}$ )/1,1-bis[(di-4-tolylamino)phenyl]cyclohexane (TAPC; 10 nm)/indium tin oxide (ITO; 150 nm), in which ultrathin TAPC serves as a typical passivation layer to passivate surface defects at the perovskite/ITO interface. Perovskite nanowires were grown inside the alumina nanochannels, using the bottom Pb nanowires as one of the precursors. The incomplete consumption of Pb nanowires led to formation of electrical contacts between perovskite and Pb (Fig. 1C and fig. S10, A and B) to facilitate charge carrier transportation. Consequently, the PNA detector exhibited superb photocurrent under illumination (fig. S11A). Figure 2D demonstrates time-dependent photocurrent response to light on/off switching. The repeatable and fast response indicates great photocurrent reproducibility. The rise and fall times of photoresponse were measured to be 40.8 and 52.0 ms (fig. S11B). Figure 2E shows the photocurrent density and responsivity as a function of light power density. The photocurrent can be fitted by the sublinear power-law relationship of

$$I = A \times P^{0.45} \quad (1)$$

where  $I$  is the photocurrent,  $A$  is a coefficient, and  $P$  denotes the light power density, respectively. As the illumination intensity increases, the photocurrent increases, whereas responsivity decreases, which agrees well with previous results in PNA photodetectors (33). Intriguingly, the responsivity can reach up to 2.9 A/W when the illumination power density is reduced to 2.3  $\mu\text{W}/\text{cm}^2$ , validating the excellent sensitivity of the PNA photodetector in a dim environment. To evaluate the photoresponse of the PNA detector toward different optical wavelengths, we measured the spectral responsivity (fig. S11C), which



Movie 1. Overview of a biomimetic PHCE for robot vision.

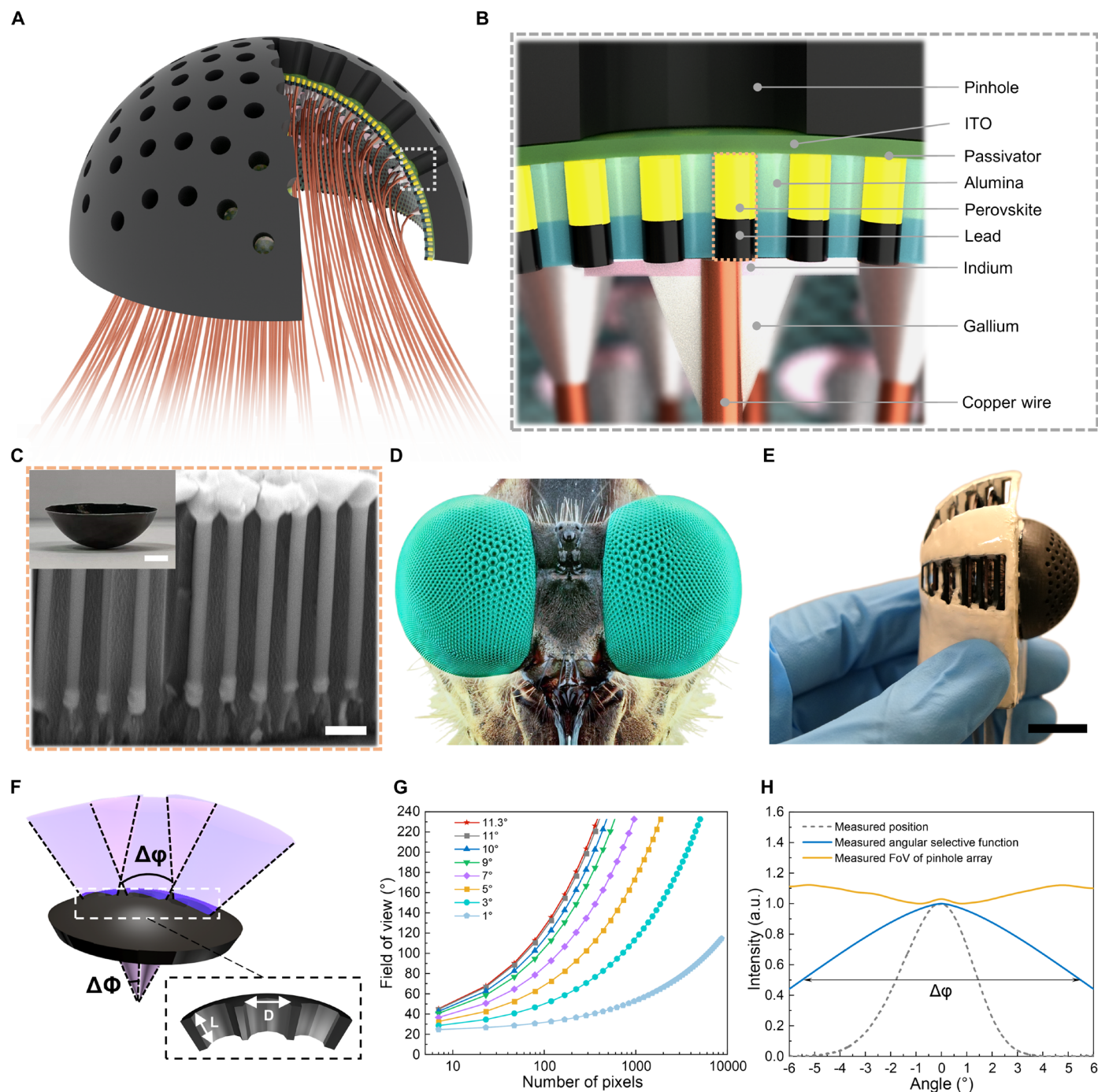


**Fig. 1. Schematic illustration and images of PHCE camera and integrated components.** (A) Illustration of PHCE integral structure. (B) Exploded view of PHCE system [magnified plot of gray frame in (A)]. (C) Cross-sectional SEM image of perovskite nanowires in hemispherical PAM [located in area highlighted by orange frame in (B)]. Scale bar, 1  $\mu\text{m}$ . Inset shows photograph of hemispherical PAM with perovskite inside. Scale bar, 5 mm. (D) Macro photograph of a robber fly's eye. (E) Side-view photograph of PHCE system mounted on PCBs. Scale bar, 1 cm. (F) Cross-sectional illustration of three adjacent pinhole units with the marked key parameters:  $\Delta\phi$ ,  $\Delta\Phi$ , the diameter ( $D$ ), and length ( $L$ ) of each pinhole. (G) Simulation of integral FoV as a function of the number of pinhole pixels with different  $\Delta\Phi$  values. (H) Normalized intensity distribution from different angles for single pinhole and pinhole array of three pinholes. Inset shows the calculated  $\Delta\phi$ .

reveals a broadband response with a distinct cutoff edge at 798 nm. We also conducted the stability and repeatability test on single-pixel PNA detectors. As shown in Fig. 2E, nonencapsulated devices retain more than 80% of the original photoresponse after being stored in an ambient environment for 10 months. Moreover, we

observed nearly no performance degradation after tracking the on/off switching behavior for more than 4000 s (fig. S11D), indicating excellent operational stability. We further examined the responsivity distribution of each pixel in the photodetector array as plotted in fig. S12 and calculated the responsivity to be  $123.6 \pm 17.4 \text{ mA/W}$

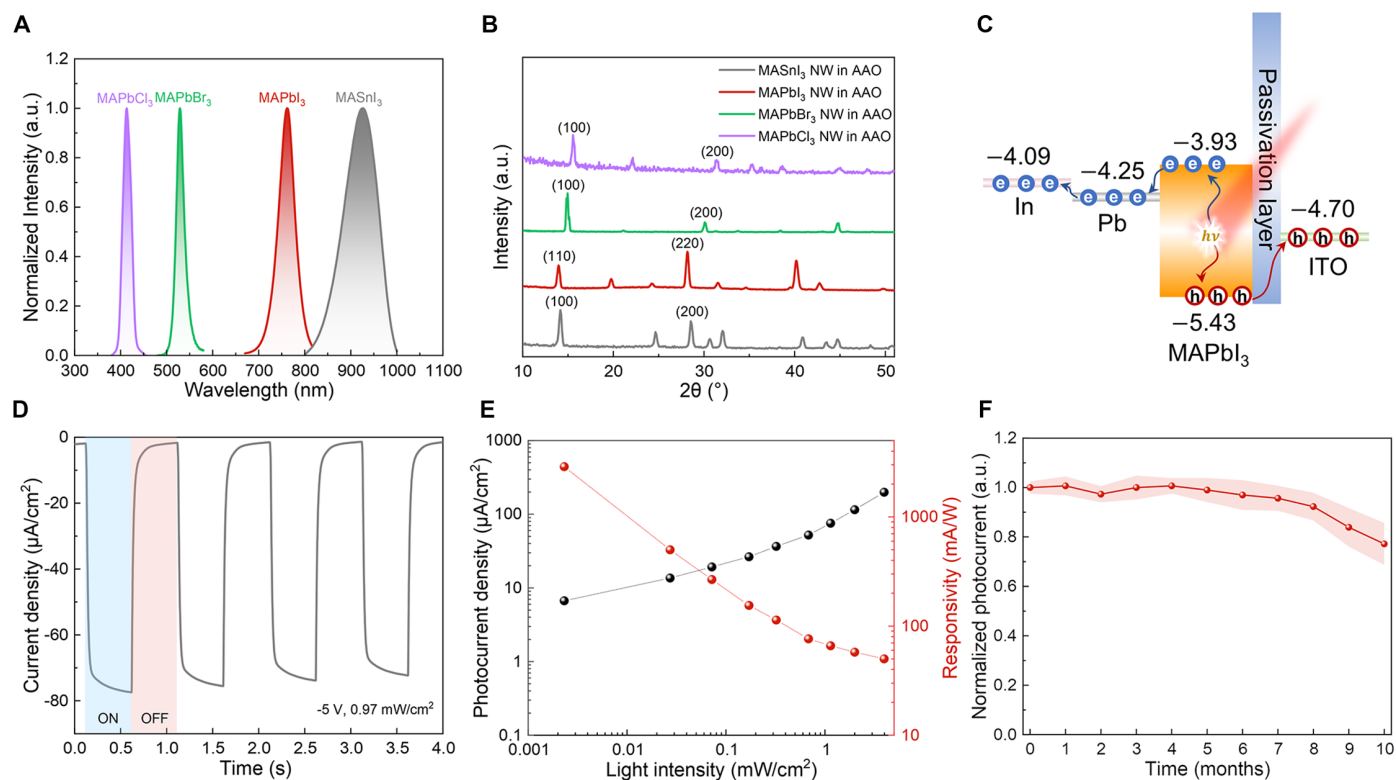


**Fig. 2. Optoelectronic performance of perovskite nanowire photodetector.** (A) Photoluminescence spectra and (B) XRD spectra of different perovskite nanowires in PAM. (C) Energy-level alignment of single-pixel MAPbI<sub>3</sub> nanowire photodetector. (D) Time-dependent on/off switching behavior under  $-5$ -V bias voltage with a light intensity of  $0.97$  mW/cm<sup>2</sup>. (E) Illumination intensity-dependent photocurrent density and responsivity of a single-pixel photodetector. The weakest light intensity is  $2.3$   $\mu$ W/cm<sup>2</sup>. (F) Statistic photocurrent evolution of single-pixel photodetectors without encapsulation. The light source used for photodetection was a halogen lamp. Points represent mean values, and shading represents SD for six independent test samples.

with a light intensity of  $0.2$  mW/cm<sup>2</sup>, therefore verifying the decent performance uniformity.

### Integrated PHCE camera for wide-angle imaging

On the basis of the respectable performance of individual pixels, we further evaluated the imaging functionality of the integrated PHCE system. Figure 3A presents a schematic of the measurement setup design, in which the total 121 ommatidia are connected to a computer-controlled multiplexer through PCBs. The captured pattern could be reconstructed via a well-programmed interface. The hemispherical geometry endows the entire system with a large FoV. As depicted in Fig. 3B, we rendered the overall FoV of the PHCE system, extracted from the direct measurement results in our custom-made setup (fig. S13, see Materials and Methods for more details). The diagonal visual field of our hemispherical PHCE is approximately  $140^\circ$ , which is consistent with the aforementioned simulation results (Fig. 1G).

To systematically demonstrate the imaging capability of PHCE, a custom-made setup was used to project different target light patterns on the device (fig. S14). Figure 3C shows the captured image of a circular pattern under convergent light. It is worth pointing out that the cross-talk issue can be notably suppressed in our device owing to the electric insulation property among well-defined PAM channels (32, 34). We further demonstrated that the PHCE system could image objects simultaneously within a wide

visual angle. Figure 3D shows that a green cross and a red triangle pattern generated by convergent light can be accurately captured and easily recognized using our device. To validate this, we also conducted imaging simulations on our vision system. The simulated results correspond well with the experimentally obtained patterns (fig. S15, A to D). Moreover, we provided simulated images of different capital letters (fig. S15E), thus verifying the imaging capability of the PHCE system without any mechanical movement. We further captured different patterns shining from different angles under parallel light (fig. S16). Only patterns within a limited angle could be observed, thus confirming the device's good angular selectivity.

### Target positioning and motion tracking with PHCE camera

Biological compound eyes (for example, in flies, ants, and working bees) suffer from limited resolution and poor imaging quality (35). However, they are specialized in movement perception. To emulate the real function of insects' compound eyes, we fabricated a carefully designed 37-ommatidia ( $L/D = 2.5$ ,  $\Delta\Phi = 20^\circ$ ) PHCE system and used a point light source as the object. Optical simulations were performed to ascertain the suitability of these parameters for the 37-ommatidia configuration, as depicted in figs. S17 and S18. In our case, when the point light source moves away from PHCE, the illuminated area increases, thus more pixels are activated, and vice versa. In addition, when the point source moves toward other directions,

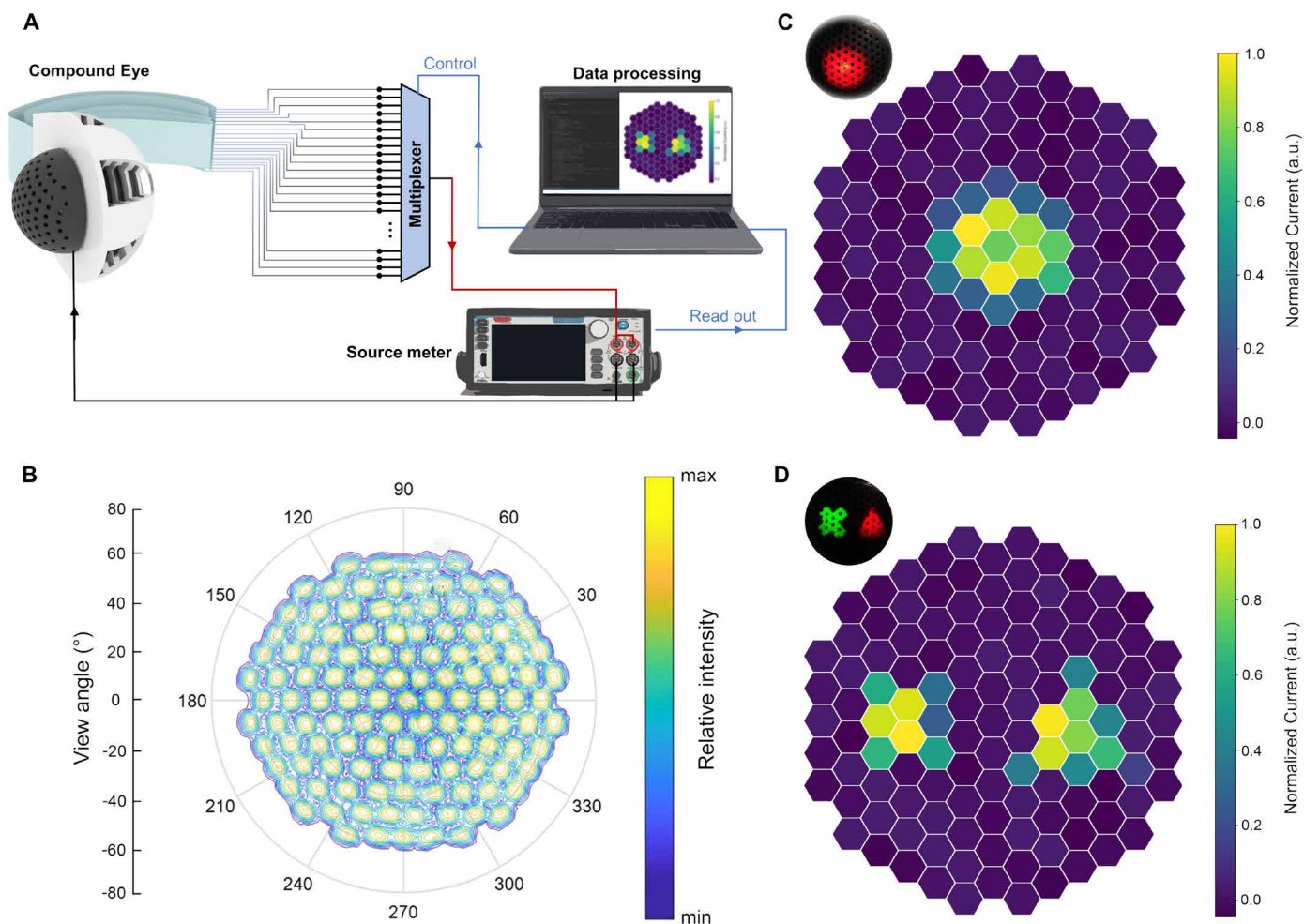


**Fig. 3. Imaging capability of PHCE camera.** (A) Schematic illustration of the measurement setup. (B) Measured FoV for the hemispherical imaging system. (C) Captured image of circular pattern. (D) Captured image of cross and triangular patterns. Insets provide optical photos of patterns. The light source used for imaging was convergent light.

the synclastic pixels respond. To accurately position a 3D moving trajectory of a point light source, we further constructed a dual-eyed system presented in Fig. 4A, in which the angle between two PHCEs was fixed at  $60^\circ$  and the overall FoV increased to  $220^\circ$ . The whole system was connected to a computer-controlled multiplexer, and the real-time data were collected via programming. Figure 4B depicts the working principle of this binocular system, in which the entire zone can be divided into three parts, namely, blind zone, motion-detecting zone, and precise positioning zone. To understand the positioning mechanism, we conducted optical simulations in different zones. The movement could be detected in the motion-detecting zone (fig. S19 and Supplementary Methods). Concurrently, optical simulation results (fig. S20) in the precise positioning zone indicate that we can position an “S”-shape trajectory of a moving point light source along a fixed plane. On this basis, we randomly moved a point source in the positioning zone and recorded nodes with the binocular system. Typical binocular images captured at different positions (marked with red stars in Fig. 4C) are listed in fig. S21. We further resolved these positions and reconstructed the trajectory in the 3D space as

plotted in Fig. 4C (see more details in Supplementary Methods), which verifies the target positioning capability of the PHCE system.

Inspired by living insects, we merged a monocular PHCE with integrated circuits for onboard signal collecting, processing, and wireless communication (figs. S22 and S23). Owing to the excellent angular selectivity of our system, we further installed it on a commercial drone with an open-code control to execute the real-time motion tracking of a quadruped robot equipped with a point light source. Figure 4D illustrates the schematic of the integrated system's working principle. Specifically, the mounted PHCE senses the light signal and transmits it to the control unit on the drone for signal processing, in which the signal is further processed. Last, the control unit issues movement instructions to the drone according to the relative position change between the drone in the air and the quadruped robot on the ground. In this case, we could achieve a frame rate of approximately 25 Hz, which is currently limited by the response time of the PNA detector; however, it can be further improved in the future. The drone is controlled by a tunable proportional, integral, and derivative (PID) algorithm. Figure 4E displays the photograph of the

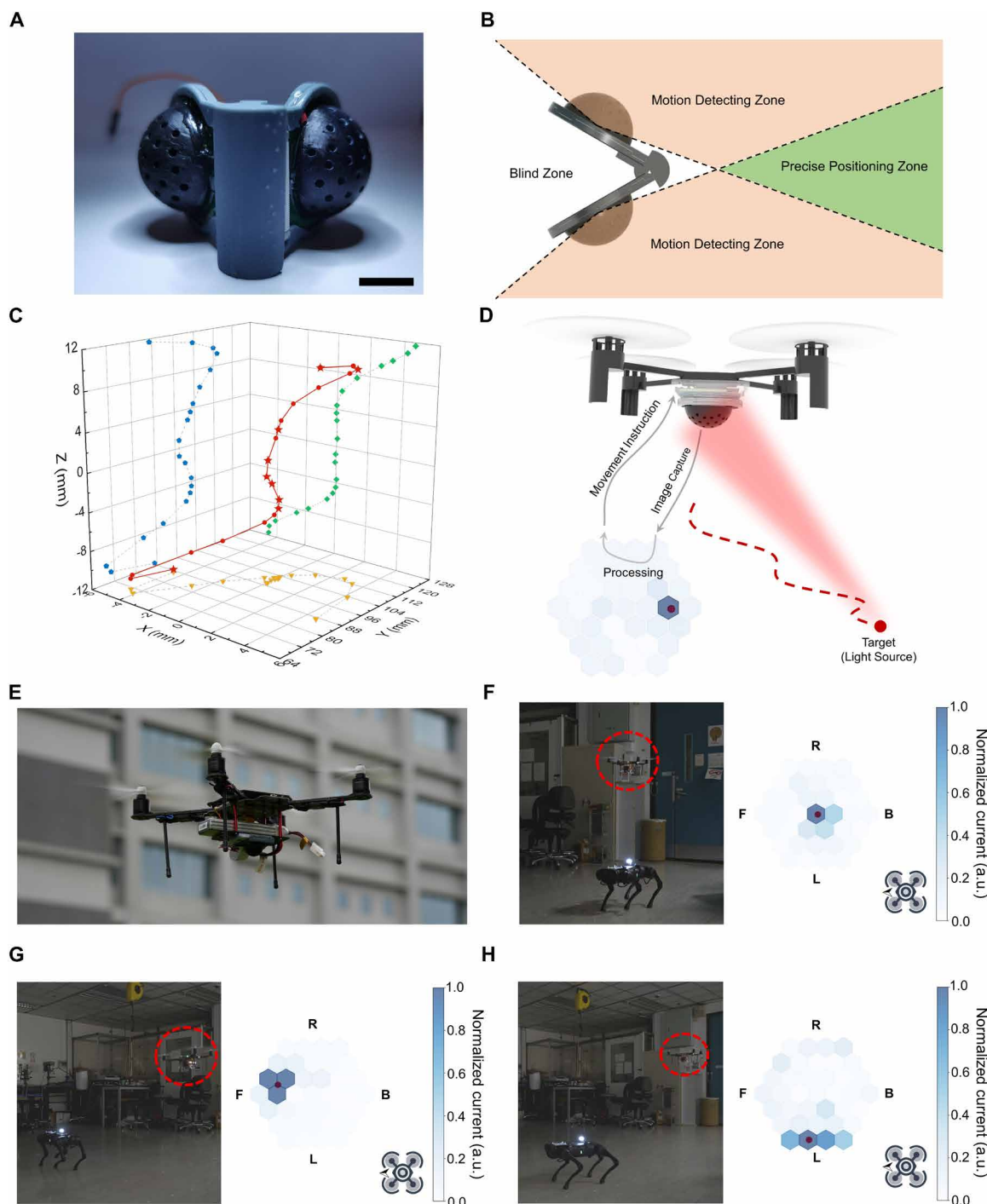


**Fig. 4. Target positioning and on-drone motion tracking of PHCE system.** (A) Photograph of binocular vision system comprising two PHCEs. Scale bar, 1 cm. (B) Working principle of the binocular vision system. (C) Calculated spatial positions and generated movement path of a moving point light source in 3D space. (D) Working principle of on-drone motion tracking. (E) Photographs of on-drone PHCE. (F to H) Photographs of light source and drone during movement and corresponding images captured by on-drone PHCE. The inset icon represents the forward direction. F, B, R, and L represent front, back, right, and left, respectively.

drone integrated with the PHCE system, in which the PHCE is secured by a 3D-printed holder. Integrated with our PHCE, the drone successfully tracked the continuous motion of the quadruped robot (installed with a white light source) along a square path (Movie 2). We further compared the digital images with the current maps

captured at different moments (Fig. 4, F to H, and fig. S24). The consistency strongly substantiates the tracking accuracy and repeatability of this fully integrated system. To highlight the unique features of our PHCE, we compared the key specifications of previously reported artificial compound eyes, as listed in table S2.



**Movie 2. Motion tracking of the on-drone PHCE vision system.** A white spotlight installed on a moving quadruped robot is detected and traced by the on-drone PHCE along a square trajectory.

## DISCUSSION

Biological compound vision systems, featuring extraordinary imaging capability (for example, ultrawide FoV and outstanding angular selectivity), have garnered extensive interest in both basic research and practical applications. To mimic their unique characteristics, conventional artificial compound eyes have been developed with complex lens systems and commercial planar imagers (36, 37). To achieve larger FoV and reduced optical aberration, hemispherical imagers have been integrated with microlens array owing to deformable electronics (19, 38). To address the challenges of structural instability and limited pixels, in this study, we developed a pinhole compound vision system for wide-range imaging and accurate target positioning, enabled by the following features: an inherent hemispherical PNA imager with high pixel density to enlarge the imaging field and a 3D-printed lens-free pinhole array with a customizable layout to regulate incident light and eliminate the blind area between neighboring ommatidia. Last, we integrated the PHCE system with a programmable drone to realize real-time in-air motion tracking of a ground robot.

Our fully integrated PHCE has shown potential as an advanced vision system for a wide range of applications, particularly in robotics. Considering practical applications, the current PHCE system could be improved by, for instance, exploring higher-density back contact, using rational scanning methods and algorithms for high-resolution and infinite depth-of-field imaging, engineering perovskites for improved sensitivity and faster motion detection, optimizing the optical design for amphibious vision, and developing varied geometries and layouts for extending the functionality of the device. First, the pixel density of the current device is limited by manually handled back contact connections. Natural compound eyes function effectively with hundreds of ommatidia (table S1). With the aid of robotic programming or microneedle-array socket, thousands of pixels can be potentially realized, which will further enhance angular selectivity and improve imaging resolution. In addition, rotating and scanning methods can be used to improve the effective

resolution based on limited pixel numbers. In addition, well-established compressed sensing techniques can provide several-fold improvement in imaging resolution (figs. S25 to S27 and Supplementary Methods), and the pinhole imaging quality can be further improved by virtue of advanced algorithms (39–41). Second, compound eyes are widely regarded as a powerful tool to detect high-speed motion. The current PNA detector based on a single component exhibits a millisecond-level response time. However, through compositional and interfacial engineering, perovskite photodetectors with ultrafast response time (down to the nanosecond level) and high sensitivity to ultralow light intensity (down to the picowatts level) can be obtained (42, 43), thus surpassing the response time and sensitivity of animals' eyes. In this case, the PHCE system can detect and track ultrafast movements, even in ultralow-light environments. Given its simple lens-free

and self-encapsulation configuration, our imaging system can, in principle, adapt to both terrestrial and aquatic environments with fine optical design (fig. S28). Last, because of the tunable geometries and layouts of the 3D-printed pinhole optical structure and the moldable underlying curvy imagers, the PHCE system can be further upgraded to realize more sophisticated functions in the future.

Overall, inspired by insects' compound eye systems, we have designed and fabricated a unique PHCE system with an expansive FoV, accurate target positioning, and dynamic motion tracking capability. With further improvements in the future, including miniaturizing the device size and increasing the number of ommatidia, imaging resolution, and response speed, this type of device can find broad applications in optoelectronics and robotics.

## MATERIALS AND METHODS

### Optical simulation for design of pinhole array

Monte Carlo–based 3D ray-tracing software (OpticStudio 16.0, Radiant ZEMAX) was exploited to design the size and layout of the pinhole array system. In the nonsequential mode, a spherical surface with a radius of 10 mm and an aperture of 20 mm was used to simulate the distribution of the photodetector. In the simulation environment, the smallest element on the spherical surface was 0.2 mm by 0.6 mm to ensure enough resolution for the imaging. Another cladding sphere was set in the extended direction from the sphere center. The pinhole was set by cylinder volume with various conditions, followed by the array ring in ZEMAX, to achieve proper distribution of the pinhole array. Light sources with different shapes, positions, and tilted angles of the surface were simulated to get the FoV and blind zone information of the pinhole array. A numeric computational environment developed by MathWorks (MATLAB) was used to calculate the transmittance versus angle, its diacritical acceptance angle, and FoV.

### Fabrication and characterization of pinhole array

According to the 3D modeling, the pinhole array and matched masks were fabricated by 3D printing with a printing resolution of 10  $\mu\text{m}$  (nanoArch P140, BMF Precision Tech Inc.). For the optical test of the pinhole array, it was mechanically rotated in 2D (azimuthal and polar) to obtain transmittance at different angles (fig. S13). The FoV of the pinhole array was tested under white light illumination. The rotational step is  $2^\circ$  for this 2D measurement. The measurement range is from  $-80^\circ$  to  $80^\circ$  and  $360^\circ$  for the polar angle and azimuthal angle, respectively. A more accurate measurement for only polar rotation was characterized by a collimated and expanded laser beam (532 nm) with a rotational step of  $0.1^\circ$ . With the assistance of the beam expansion, all the pinholes on the sphere were illuminated by the laser, but only the selected angle range was transmitted through the pinhole array. The transmitted light was focused on the detector to collect all the light intensity. Laser beam expansion is critical for the measurement of FoV. The unexpanded laser spot is smaller than the aperture size of a pinhole, so the measured FoV of a single pinhole is smaller than the actual value and can only represent the distribution of the pinhole positions.

### Fabrication of hemispherical PNA image sensor

The fabrication of the PNA imager started with a hemispherical aluminum (Al) shell, which was stamped out from a 500- $\mu\text{m}$ -thick Al sheet via designed hemispherical molds. After electropolishing the Al shell, we set a standard two-step anodization process to fabricate a 5- $\mu\text{m}$ -thick PAM with a pitch of 500 nm. The diameter of the PAM nanochannel can be enlarged to about 300 nm by a wet chemical etching process. Then, a barrier thinning and Pb electro-deposition were performed to form a 2- $\mu\text{m}$ -long Pb nanowire array in the PAM channels. Next, the chip was transferred into a tube furnace to grow 4- $\mu\text{m}$ -long perovskite nanowires with different compositions inside the PAM. We then carried out an ion-milling process to remove the overgrown layer and a subsequent regrowth process to improve the PNA quality. A 10-nm-thick TAPC layer was evaporated on the PNA surface to serve as a passivation and electron-blocking layer. After that, a 150-nm-thick ITO was sputtered on the TAPC layer to serve as the common electrode. Before etching the bottom Al to get a free-standing device, an ultrathin ultraviolet (UV) epoxy layer was coated on the top by a drop-casting method to protect the whole device. We used sodium hydroxide and mercury chloride solution to etch away the residual Al and obtain the free-standing hemispherical chip. Then, an In back contact was evaporated on the concave side with a porous mask. Enamelled copper (Cu) wires were attached to the isolated In surface with the assistance of Ga liquid metal under the spatial confinement of a thicker porous mask. After bonding, UV epoxy was injected and cured to seal the device.

### Characterization of material and photodetector

A field-emission scanning electron microscope (JSM-7100F, JEOL) was used to characterize the PAM and PNA morphology and the corresponding energy-dispersive x-ray mapping. Steady-state photoluminescence measurements for different perovskite nanowires were carried out on an Edinburgh FS5 fluorescence spectrometer. XRD patterns of perovskite nanowires were obtained with a PANalytical x-ray diffractometer (X'pert Pro). A transmission electron microscope (TEM-2010F, JEOL) was used with a 200-kV acceleration voltage to get high-resolution images

of a single perovskite nanowire. The current-time and current-voltage curves of individual pixels were measured on the probe station (Signatone) equipped with a semiconductor parameter analyzer (HP4156A, Agilent B1500A) with neutral-density filters to adjust the light intensity. The light intensity was calibrated with an optical power meter (PM100D, Thorlabs). An additional chopper was used to chop light into square wave optical signals with different frequencies. All the optoelectronic measurements were performed in an ambient environment (at  $\sim 23^\circ$  to  $28^\circ\text{C}$  and  $\sim 45$  to 55% relative humidity).

### Integration of PHCE system

The hemispherical PNA imager was assembled with the pinhole array optical structure referring to the reserved markers at the edge, and the epoxy was used to enhance the adhesion and further seal the device. On the concave side, Cu wires were bonded on PCBs cycle by cycle. Three-dimensionally printed brackets were used to fix and combine all the PCBs. On the convex side, the ITO layer was bonded with conductive wires in advance using silver paste. Both monocular and binocular systems were assembled in this way and eventually fixed by a 3D-printed model.

### Wide-angle imaging and target positioning demonstration

We first demonstrated wide-angle imaging with a single 121-pixel PHCE. The PHCE was connected to the source meter unit (Keithley 2450) through one 128-channel multiplexer unit (PXI2530B, National Instruments, USA), which was installed inside a chassis (PXI1031, National Instruments, USA). The whole system was controlled by a homebuilt Python program. Next, we integrated two 37-pixel PHCEs, which were fixed to a 3D-printed bracket with an angle of  $60^\circ$ , to demonstrate target positioning. The measuring system was identical to that used in the wide-angle imaging demonstration.

### Motion tracking demonstration

We mounted a 37-pixel PHCE on an open-source drone (ANO Technology&Creation) to verify the motion-tracking capability. The data were collected by customized designed PCB and transmitted to the drone. To test the motion tracking, we controlled a quadruped robot (Model A1, Unitree) loaded with a light source to transit along different paths in a low-light indoor environment.

### Statistical analysis

We used mean values ( $\pm$  SD) to quantify the responsivity of the PNA photodetector ( $N = 121$ ) and the 10-month photocurrent stability of single-pixel photodetectors ( $N = 6$ ).

### Supplementary Materials

This PDF file includes:

Methods  
Figs. S1 to S28  
Tables S1 to S4  
References (44–55)

Other Supplementary Material for this manuscript includes the following:

MDAR Reproducibility Checklist

### REFERENCES AND NOTES

1. M. F. Land, D.-E. Nilsson, *Animal Eyes* (Oxford Univ. Press, ed. 2, 2012).

2. K. Kirschfeld, The resolution of lens and compound eyes, in *Neural Principles in Vision*, F. Zettler, R. Weiler, Eds. (Springer, 1976), pp. 354–370.
3. D. Floreano, J.-C. Zufferey, M. V. Srinivasan, C. Ellington, *Flying Insects and Robots* (Springer, 2009).
4. X. Gao, X. Yan, X. Yao, L. Xu, K. Zhang, J. Zhang, B. Yang, L. Jiang, The dry-style antifogging properties of mosquito compound eyes and artificial analogues prepared by soft lithography. *Adv. Mater.* **19**, 2213–2217 (2007).
5. D. Kang, C. Pang, S. M. Kim, H. S. Cho, H. S. Um, Y. W. Choi, K. Y. Suh, Shape-controllable microlens arrays via direct transfer of photocurable polymer droplets. *Adv. Mater.* **24**, 1709–1715 (2012).
6. J. Li, W. Wang, X. Mei, D. Hou, A. Pan, B. Liu, J. Cui, Fabrication of artificial compound eye with controllable field of view and improved imaging. *ACS Appl. Mater. Interfaces* **12**, 8870–8878 (2020).
7. K.-H. Jeong, J. Kim, L. P. Lee, Biologically inspired artificial compound eyes. *Science* **312**, 557–561 (2006).
8. Z.-Y. Hu, Y.-L. Zhang, C. Pan, J.-Y. Dou, Z.-Z. Li, Z.-N. Tian, J.-W. Mao, Q.-D. Chen, H.-B. Sun, Miniature optoelectronic compound eye camera. *Nat. Commun.* **13**, 5634 (2022).
9. D. Wu, J.-N. Wang, L.-G. Niu, X. L. Zhang, S. Z. Wu, Q.-D. Chen, L. P. Lee, H. B. Sun, Bioinspired fabrication of high-quality 3D artificial compound eyes by voxel-modulation femtosecond laser writing for distortion-free wide-field-of-view imaging. *Adv. Opt. Mater.* **2**, 751–758 (2014).
10. T. Gissibl, S. Thiele, A. Herkommer, H. Giessen, Two-photon direct laser writing of ultracompact multi-lens objectives. *Nat. Photonics* **10**, 554–560 (2016).
11. H. Liu, Y. Huang, H. Jiang, Artificial eye for scotopic vision with bioinspired all-optical photosensitivity enhancer. *Proc. Natl. Acad. Sci. U.S.A.* **113**, 3982–3985 (2016).
12. H. Bian, Y. Wei, Q. Yang, F. Chen, F. Zhang, G. Du, J. Yong, X. Hou, Direct fabrication of compound-eye microlens array on curved surfaces by a facile femtosecond laser enhanced wet etching process. *Appl. Phys. Lett.* **109**, 221109 (2016).
13. J.-J. Cao, Z.-S. Hou, Z.-N. Tian, J.-G. Hua, Y.-L. Zhang, Q.-D. Chen, Bioinspired zoom compound eyes enable variable-focus imaging. *ACS Appl. Mater. Interfaces* **12**, 10107–10117 (2020).
14. B. Dai, L. Zhang, C. Zhao, H. Bachman, R. Becker, J. Mai, Z. Jiao, W. Li, L. Zheng, X. Wan, T. J. Huang, S. Zhuang, D. Zhang, Biomimetic composition compound eye fabricated using microfluidic-assisted 3D printing. *Nat. Commun.* **12**, 6458 (2021).
15. T. Gissibl, S. Thiele, A. Herkommer, H. Giessen, Sub-micrometre accurate free-form optics by three-dimensional printing on single-mode fibres. *Nat. Commun.* **7**, 11763 (2016).
16. S. Thiele, K. Arzenbacher, T. Gissibl, H. Giessen, A. M. Herkommer, 3D-printed eagle eye: Compound microlens system for foveated imaging. *Sci. Adv.* **3**, e1602655 (2017).
17. H. C. Ko, M. P. Stoykovich, J. Song, V. Malyarchuk, W. M. Choi, C.-J. Yu, J. B. Geddes Iii, J. Xiao, S. Wang, Y. Huang, J. A. Rogers, A hemispherical electronic eye camera based on compressible silicon optoelectronics. *Nature* **454**, 748–753 (2008).
18. D. Floreano, R. Pericet-Camara, S. Viollet, F. Ruffier, A. Brückner, R. Leitl, W. Buss, M. Menouni, F. Expert, R. Juston, M. K. Dobrzynski, G. L'Eplattenier, F. Reckenwald, H. A. Mallot, N. Franceschini, Miniature curved artificial compound eyes. *Proc. Natl. Acad. Sci. U.S.A.* **110**, 9267–9272 (2013).
19. Y. M. Song, Y. Xie, V. Malyarchuk, J. Xiao, I. Jung, K.-J. Choi, Z. Liu, H. Park, C. Lu, R.-H. Kim, R. Li, K. B. Crozier, Y. Huang, J. A. Rogers, Digital cameras with designs inspired by the arthropod eye. *Nature* **497**, 95–99 (2013).
20. K. Sim, S. Chen, Z. Li, Z. Rao, J. Liu, Y. Lu, S. Jang, F. Ershad, J. Chen, J. Xiao, C. Yu, Three-dimensional curvy electronics created using conformal additive stamp printing. *Nat. Electron.* **2**, 471–479 (2019).
21. K. Zhang, Y. H. Jung, S. Mikael, J.-H. Seo, M. Kim, H. Mi, H. Zhou, Z. Xia, W. Zhou, S. Gong, Z. Ma, Origami silicon optoelectronics for hemispherical electronic eye systems. *Nat. Commun.* **8**, 1782 (2017).
22. Z. Rao, Y. Lu, Z. Li, K. Sim, Z. Ma, J. Xiao, C. Yu, Curvy, shape-adaptive imagers based on printed optoelectronic pixels with a kirigami design. *Nat. Electron.* **4**, 513–521 (2021).
23. M. Lee, G. J. Lee, H. J. Jang, E. Joh, H. Cho, M. S. Kim, H. M. Kim, K. M. Kang, J. H. Lee, M. Kim, H. Jang, J.-E. Yeo, F. Durand, N. Lu, D.-H. Kim, Y. M. Song, An amphibious artificial vision system with a panoramic visual field. *Nat. Electron.* **5**, 452–459 (2022).
24. F. Expert, F. Ruffier, Flying over uneven moving terrain based on optic-flow cues without any need for reference frames or accelerometers. *Bioinspir. Biomim.* **10**, 026003 (2015).
25. G. C. H. E. de Croon, J. J. G. Dupuyroux, S. B. Fuller, J. A. R. Marshall, Insect-inspired AI for autonomous robots. *Sci. Robot.* **7**, eab6334 (2022).
26. M. F. Land, Visual acuity in insects. *Annu. Rev. Entomol.* **42**, 147–177 (1997).
27. A. Waleed, M. M. Tavakoli, L. Gu, Z. Wang, D. Zhang, A. Manikandan, Q. Zhang, R. Zhang, Y.-L. Chueh, Z. Fan, Lead-free perovskite nanowire array photodetectors with drastically improved stability in nanoengineering templates. *Nano Lett.* **17**, 523–530 (2017).
28. A. Waleed, M. M. Tavakoli, L. Gu, S. Hussain, D. Zhang, S. Poddar, Z. Wang, R. Zhang, Z. Fan, All inorganic cesium lead iodide perovskite nanowires with stabilized cubic phase at room temperature and nanowire array-based photodetectors. *Nano Lett.* **17**, 4951–4957 (2017).
29. D. Zhang, Q. Zhang, B. Ren, Y. Zhu, M. Abdellah, Y. Fu, B. Cao, C. Wang, L. Gu, Y. Ding, K.-H. Tsui, S. Fan, S. Poddar, L. Shu, Y. Zhang, D.-B. Kuang, J.-F. Liao, Y. Lu, K. Zheng, Z. He, Z. Fan, Large-scale planar and spherical light-emitting diodes based on arrays of perovskite quantum wires. *Nat. Photonics* **16**, 284–290 (2022).
30. Y. Fu, S. Poddar, B. Ren, Y. Xie, Q. Zhang, D. Zhang, B. Cao, Y. Tang, Y. Ding, X. Qiu, L. Shu, J.-F. Liao, D.-B. Kuang, Z. Fan, Strongly quantum-confined perovskite nanowire arrays for color-tunable blue-light-emitting diodes. *ACS Nano* **16**, 8388–8398 (2022).
31. D. Zhang, Q. Zhang, Y. Zhu, S. Poddar, Y. Zhang, L. Gu, H. Zeng, Z. Fan, Metal halide perovskite nanowires: Synthesis, integration, properties, and applications in optoelectronics. *Adv. Energy Mater.* **13**, 2201735 (2022).
32. Z. Long, X. Qiu, C. L. J. Chan, Z. Sun, Z. Yuan, S. Poddar, Y. Zhang, Y. Ding, L. Gu, Y. Zhou, W. Tang, A. K. Srivastava, C. Yu, X. Zou, G. Shen, Z. Fan, A neuromorphic bionic eye with filter-free color vision using hemispherical perovskite nanowire array retina. *Nat. Commun.* **14**, 1972 (2023).
33. L. Gu, S. Poddar, Y. Lin, Z. Long, D. Zhang, Q. Zhang, L. Shu, X. Qiu, M. Kam, A. Javey, Z. Fan, A biomimetic eye with a hemispherical perovskite nanowire array retina. *Nature* **581**, 278–282 (2020).
34. Y. Ding, G. Liu, Z. Long, Y. Zhou, X. Qiu, B. Ren, Q. Zhang, C. Chi, Z. Wan, B. Huang, Z. Fan, Uncooled self-powered hemispherical biomimetic pit organ for mid- to long-infrared imaging. *Sci. Adv.* **8**, eabq8432 (2022).
35. L. Zhang, H. Zhan, X. Liu, F. Xing, Z. You, A wide-field and high-resolution lensless compound eye microsystem for real-time target motion perception. *Microsyst. Nanoeng.* **8**, 83 (2022).
36. G. J. Lee, C. Choi, D.-H. Kim, Y. M. Song, Bioinspired artificial eyes: Optic components, digital cameras, and visual prostheses. *Adv. Funct. Mater.* **28**, 1705202 (2018).
37. Q. Yang, M. Li, H. Bian, J. Yong, F. Zhang, X. Hou, F. Chen, Bioinspired artificial compound eyes: Characteristic, fabrication, and application. *Adv. Mater. Technol.* **6**, 2100091 (2021).
38. H. L. Phan, J. Yi, J. Bae, H. Ko, S. Lee, D. Cho, J.-M. Seo, K.-i. Koo, Artificial compound eye systems and their application: A review. *Micromachines* **12**, 847 (2021).
39. W.-B. Lee, H. Jang, S. Park, Y. M. Song, H.-N. Lee, COMPU-EYE: A high resolution computational compound eye. *Opt. Express* **24**, 2013–2026 (2016).
40. W.-B. Lee, H.-N. Lee, Depth-estimation-enabled compound eyes. *Opt. Commun.* **412**, 178–185 (2018).
41. J. D. Rego, H. Chen, S. Li, J. Gu, S. Jayasuriya, Deep camera obscura: An image restoration pipeline for pinhole photography. *Opt. Express* **30**, 27214–27235 (2022).
42. A. Morteza Najarian, M. Vafaie, A. Johnston, T. Zhu, M. Wei, M. I. Saidaminov, Y. Hou, S. Hoogland, F. P. García de Arquer, E. H. Sargent, Sub-millimetre light detection and ranging using perovskites. *Nat. Electron.* **5**, 511–518 (2022).
43. Y. Fang, J. Huang, Resolving weak light of sub-picowatt per square centimeter by hybrid perovskite photodetectors enabled by noise reduction. *Adv. Mater.* **27**, 2804–2810 (2015).
44. M. A. Zezeera, P. Tichit, G. S. Balamurali, E. Baird, A. Kelber, H. Somanathan, Spatial resolution and sensitivity of the eyes of the stingless bee, *Tetragona iridipennis*. *J. Comp. Physiol. A Neuroethol. Sens. Neural Behav. Physiol.* **208**, 225–238 (2022).
45. M. F. Land, G. Gibson, J. Horwood, J. Zeil, Fundamental differences in the optical structure of the eyes of nocturnal and diurnal mosquitoes. *J. Comp. Physiol. A* **185**, 91–103 (1999).
46. H. Kawada, H. Tatsuta, K. Arikawa, M. Takagi, Comparative study on the relationship between photoperiodic host-seeking behavioral patterns and the eye parameters of mosquitoes. *J. Insect Physiol.* **52**, 67–75 (2006).
47. K. C. Lee, Q. Yu, U. Erb, Mesostructure of ordered corneal nano-nipple arrays: The role of 5–7 coordination defects. *Sci. Rep.* **6**, 28342 (2016).
48. D. G. Stavenga, M. Kinoshita, E. C. Yang, K. Arikawa, Retinal regionalization and heterogeneity of butterfly eyes. *Naturwissenschaften* **88**, 477–481 (2001).
49. D.-e. Nilsson, R. Odselius, Regionally different optical systems in the compound eye of the water-flea *Polyphemus* (Cladocera, Crustacea). *Proc. R. Soc. Lond. Ser. B* **217**, 163–175 (1983).
50. W. Pix, J. M. Zanker, J. Zeil, The optomotor response and spatial resolution of the visual system in male *Xenos vesparum* (Strepsiptera). *J. Exp. Biol.* **203**, 3397–3409 (2000).
51. T. J. Wardill, S. T. Fabian, A. C. Pettigrew, D. G. Stavenga, K. Nordström, P. T. Gonzalez-Bellido, A novel interception strategy in a miniature robber fly with extreme visual acuity. *Curr. Biol.* **27**, 854–859 (2017).
52. S. Schwarz, A. Narendra, J. Zeil, The properties of the visual system in the Australian desert ant *Melophorus bagoti*. *Arthropod Struct. Dev.* **40**, 128–134 (2011).
53. N. J. Marshall, M. F. Land, T. W. Cronin, Shrimps that pay attention: Saccadic eye movements in stomatopod crustaceans. *Philos. R. Soc. B* **369**, 20130042 (2014).
54. M. Land, J. Layne, The visual control of behaviour in fiddler crabs. I. Resolution, thresholds and the role of the horizon. *J. Comp. Physiol. A* **177**, 81–90 (1995).
55. D. Keum, K.-W. Jang, D. S. Jeon, C. S. H. Hwang, E. K. Buschbeck, M. H. Kim, K.-H. Jeong, *Xenos peckii* vision inspires an ultrathin digital camera. *Light Sci. Appl.* **7**, 80 (2018).

**Acknowledgments:** We acknowledge the support from the Material Characterization and Preparation Facility (MCPF), the Center for 1D/2D Quantum Materials, and the State Key Laboratory of Advanced Displays and Optoelectronics Technologies at HKUST. **Funding:** This work was financially supported by Hong Kong Research Grant Council (16205321 and 16214619), New Cornerstone Science Foundation through the XPLOER PRIZE, the Hong Kong Alliance of Technology and Innovation through the Bank of China (Hong Kong) Science and Technology Innovation Prize, Guangdong-Hong Kong-Macao Intelligent Micro-Nano Optoelectronic Technology Joint Laboratory (2020B1212030010), and Foshan Innovative and Entrepreneurial Research Team Program (2018IT100031). **Author contributions:** Y.Z., Z.S., Y.D., and Z.F. designed the experiments, analyzed the data, and wrote the paper. Y.Z., X.Q., Y.B.C., and D.Z. fabricated the PAM, PNA, and hemispherical imager. Y.Z., X.Q., S.P., S.K., and B.R. performed the characterizations for perovskite nanowires and individual devices. Y.Z., Y.D., and Z.L. contributed to the assembly of the PHCE system. Z.S., Z.Y., and Q.Z. performed the theoretical and experimental optics. Y.D., Z.W., W.Y., and C.L.J.C. designed the control and

integrated the circuits. Y.Z., Z.S., Y.D., and Z.Y. conducted the imaging simulations and related demonstrations. H.-S.K. and M.G.L. revised the manuscript. All the authors discussed the results and commented on the manuscript. **Competing interests:** This work is protected by US Provisional Patent Application No. 63/502,922 (provisional application title: "Ultra-wide field-of-view pinhole compound eye using hemispherical nanowire array for robotic vision") filed on 18 May 2023. The authors declare that they have no other competing interests. **Data and materials availability:** The data that support the findings of this study are included in the main text and the Supplementary Materials. The source codes for MATLAB and Python are available on Zenodo at [doi.org/10.5281/zenodo.10935328](https://doi.org/10.5281/zenodo.10935328).

Submitted 23 May 2023

Accepted 17 April 2024

Published 15 May 2024

10.1126/scirobotics.adi8666